NOTE: Use these buttons to print or save the form. DO NOT use the browser tool bar.

LA-UR-06-7232

Approved for public release; distribution is unlimited.

Title: Characterization of the neutron beam profile at DANCE

Author(s): A.F. Mertz, T.A. Bredeweg, A. Couture, M. Jandel, R.C. Haight, J.M. O'Donnell, R. Reifarth, R.S. Rundberg, J.R. Tesmer, J.L. Ullmann, I. Usov, D.J. Vieira, Y. Wang, J.M. Wouters

Submitted to: DANCE collaboration

Los Alamos National Laboratory, an affirmative action/equal opportunity employer, is operated by the University of California for the U.S. Department of Energy under contract W-7405-ENG-36. By acceptance of this article, the publisher recognizes that the U.S. Government retains a nonexclusive, royalty-free license to publish or reproduce the published form of this contribution, or to allow others to do so, for U.S. Government purposes. Los Alamos National Laboratory requests that the publisher identify this article as work performed under the auspices of the U.S. Department of Energy. Los Alamos National Laboratory strongly supports academic freedom and a researcher's right to publish; as an institution, however, the Laboratory does not endorse the viewpoint of a publication or guarantee its technical correctness.

Form 836 (8/00)

Characterization of the neutron beam profile at DANCE

A.F. Mertz, T.A. Bredeweg, A. Couture, M. Jandel, R.C. Haight, J.M. O'Donnell, R. Reifarth, R.S. Rundberg, J.R. Tesmer, J.L. Ullmann, I. Usov, D.J. Vieira, Y. Wang, J.M. Wouters

October 2, 2006

1 Introduction

The Detector for Advanced Neutron Capture Experiments (DANCE) is a 4π array designed to measure nuclear-capture cross sections on milligram-size samples. DANCE measures samples of a variety of sizes, which makes it beneficial for us to understand the profile of the neutron beam that reaches the sample. The goal of this study was to characterize the DANCE beam profile by finding the relative neutron flux per unit area of the beam as a function of beam radius.

2 Experimental setup

2.1 Detector for Advanced Neutron Capture Experiments

We performed the measurements for this study using the Detector for Advanced Neutron Capture Experiments (DANCE) located at flight-path 14 of the Manuel Lujan Jr. Neutron Scattering Center at the Los Alamos Neutron Science Center (LANSCE) at Los Alamos National Laboratory (LANL). LANSCE operates an 800 MeV proton linear accelerator, and the resulting proton beam is used for proton radiography, neutron production using spallation targets, and other applications. The Lujan Center uses the proton beam to produce neutrons by spallation reactions when the protons hit a tungsten target. The beam in the Lujan Center typically operates at 100 μA. The repetition

rate of 20 Hz allows for measurement of neutron energies as low as the thermal region and as high as about 500 keV. Neutron energies were recorded using the time-of-flight (TOF) method over a 20.26 m flight path (as measured from the moderator to the sample position).

DANCE is a 4π array consisting of up to 162 barium-fluoride (BaF_2) crystals in four different shapes—all pentagonal or hexagonal—glued to photomultipliers. Each shape covers the same solid angle. Because two of the crystals must be removed in order to allow for the incoming and outgoing neutron beam pipe, only 160 crystals are actually used, reducing the overall solid-angle coverage to about 3.6π. DANCE is able to accommodate high count rates because of its high segmentation that reduces the count rate per detector.

BaF_2 is an inorganic scintillation material with fast and slow decay components. With a high density of 4.88 g/cm^3, BaF_2 has a high efficiency for detecting γ-rays between 100 keV and 10 MeV.

2.2 Gold samples

We examined six gold samples, each consisting of ^{197}Au evaporated in the shape of a disc onto a thin foil of Mylar. We chose gold because it is readily available, monoisotopic and therefore relatively inexpensive, and a common standard used in nuclear physics. The gold diameters were 2, 4, 7, 10, 15, and 20 mm, and the gold's thickness was approximately 5 kÅ. The exact thickness (see Table 1) of the gold foils was determined using Rutherford Backscattering Spectrometry (RBS) on 3 MV Tandem Pelletron Ion Accelerator at Ion Beam Materials Laboratory (IBML). The RBS measurements were performed with a 1.5 MeV H^+ beam with a beam spot size of 1.5x1.5 mm^2 (0.8x0.8 mm^2 for the sample with 2 mm diameter). The backscattered proton particles from gold the target were detected by a silicon surface barrier detector at a backward angle of 167 degrees from the incident beam direction. A small beam current of $\approx$5 nA was used during the entire measurement campaign in order to reduce beam heating effects on the Mylar substrates as well as dead time corrections. The system was calibrated with a NIST Au film standard with a thickness of 442 nm. The conversion between thickness and areal density was done assuming a gold density of 5.91x10^{22}atoms/cm^3 for both NIST standard and gold films. The estimated relative errors among the different films is less than 1%. The absolute errors are estimated to be less than 4%.

Diamter (mm)	Areal density (10^{18} atoms/cm^2)	Thickness (nm))
2	2.94	497.7
4	2.91	492.5
7	2.83	478.5
10	2.82	476.7
15	2.77	467.9
20	2.75	464.5

Table 1: Thicknesses of the gold foils used during the beam profile determinations as measured using with the Rutherford Backscattering method.

As shown in Figure 1, the Mylar was affixed to an aluminum ring, the typical sample mount for DANCE measurements. For each measurement, the aluminum sample holder was placed in a small cylinder with a diameter slightly smaller than the inner diameter of the neutron beam pipe. In order to measure the background contribution from the Mylar, we also used a sample consisting of the Mylar mounted on the aluminum holder but without any gold.

2.3 Data acquisition

The DANCE data acquisition system operates in two modes, segmented mode and continuous mode. For these measurements, we operated in the continuous mode because it offers practically no dead time and is thus the preferred mode for high count rates. In the continuous mode, the digitizers start running at a pre-defined time relative to the beginning of each beam burst and collect waveforms continuously for 250 μs.

Because 250 μs is a short looking time that only allows measurements of small energy windows, we measured each sample with three different delay times in order to obtain data on specific areas of interest in the gold spectrum. We used delays of 0, 515, and 9150 μs, after which the looking time of 250 μs began. The relationship between time-of-flight value and neutron energy is given by the relativistic energy equation,

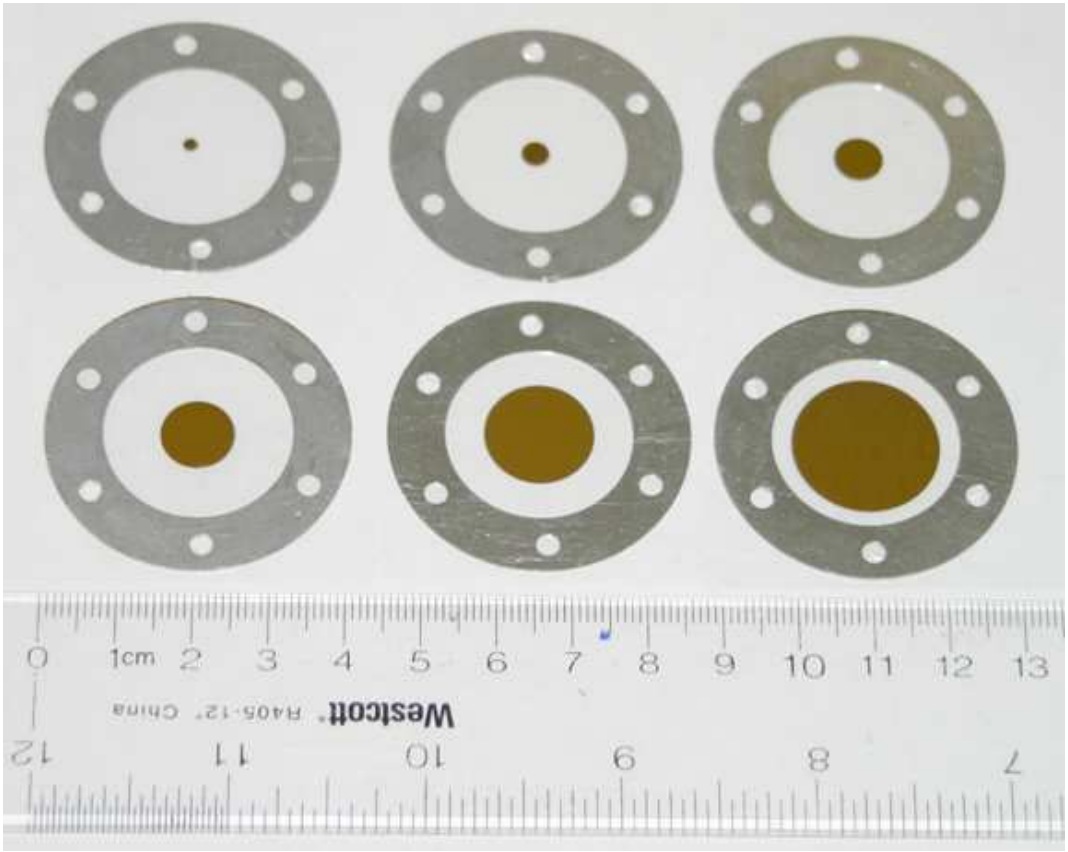

Figure 1: Gold discs with Mylar backing. The examined samples consisted of gold evaporated onto Mylar foil affixed to an aluminum ring. We examined gold discs of six different diameters, in addition to a sample without any gold (not shown).

$$E_{\text{kin}} = m_n c^2 \left[\sqrt{\frac{1}{1-\beta^2}} - 1 \right] \tag{1}$$

with

$$\beta = \frac{v}{c} = \frac{l}{tc} \,, \tag{2}$$

where E_{kin} is the neutron's kinetic energy, c is the speed of light, m_n is the mass of the neutron, $l = 20.26$ m is the length of the flight path, and t is the time of flight. The energy windows used in this study are given in Table 2 and shown in Figure 2.

t_0 (μs)	t_{f} (μs)	E_{min}	E_{max}	Au event
0	250	34.33 eV	–	60.3 eV resonance
515	765	3.67 eV	8.09 eV	4.9 eV resonance
9150	9400	24.24 meV	25.65 meV	0.025 eV thermal

Table 2: Time-of-flight windows and corresponding energy regions. Data were taken for the three time-of-flight and energy windows shown above.

We measured the samples over eleven days according to the information given in Table 3. Because the smaller gold samples by nature generated fewer counts for a given run time, we left these samples in the DANCE array for longer periods of time.

3 Data analysis and results

3.1 Total energy deposited during an event

After a neutron capture, the product nuclide is in an excited state with an excitation energy equal to the Q-value of the neutron capture reaction. The nuclide then decays in several steps to the ground state, releasing energy in the process. Typical Q-values for neutron-capture reactions are betwen 4 and 10 MeV, and ^{197}Au has a Q-value of 6.51 MeV. In order to isolate events caused by neutron capture on gold itself, we examined the total energy deposited in the detector during an event, known as the ESum. DANCE measures the total energy of a γ-decay cascade following a

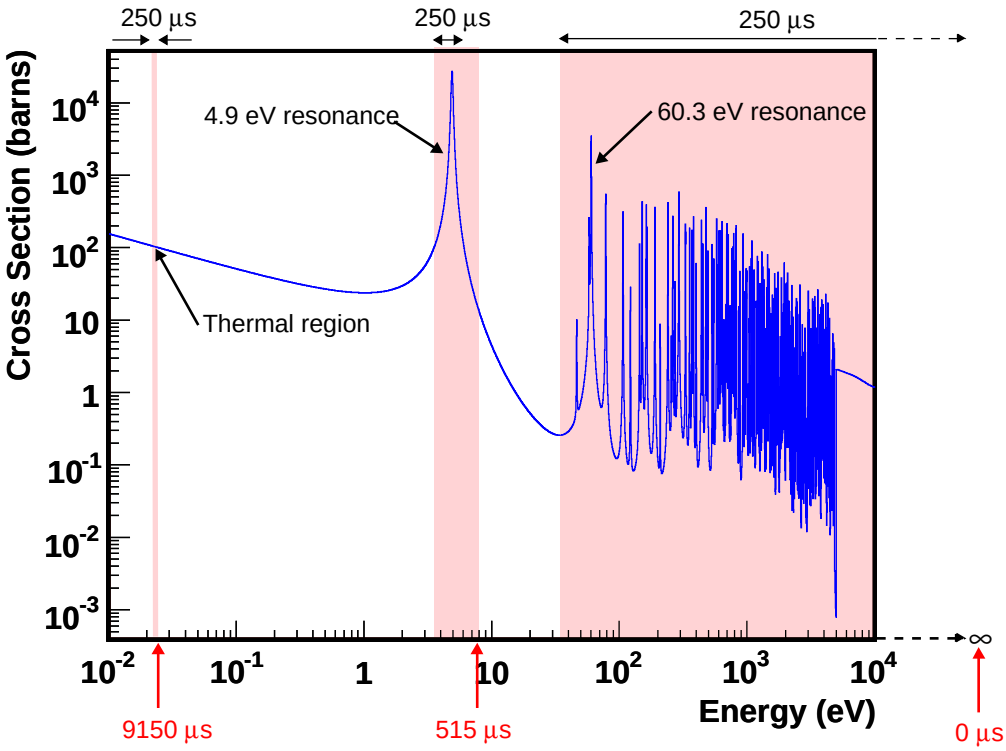

Figure 2: Time-of-flight windows for gold measurements. Shaded are the three time-of-flight energy windows measured. Each window has a time-of-flight window of 250 μs. The spectrum for gold's cross section comes from ENDF, the Evaluated Nuclear Data File.

Date	Run	Duration (hr:min)	Sample	Delay 1 (μs)	Delay 2 (μs)	Livetime (μs)
06/22/2006	7817	4:43	2 mm Au	0	515	250
06/23/2006	7818	5:55	2 mm Au	0	515	250
06/25/2006	7836	4:27	2 mm Au	0	515	250
06/25/2006	7837	4:32	2 mm Au	0	515	250
06/25/2006	7838	4:24	2 mm Au	0	515	250
06/25/2006	7839	3:39	2 mm Au	0	515	250
06/22/2006	7814	2:21	2 mm Au	515	9150	250
06/22/2006	7815	2:18	2 mm Au	515	9150	250
06/22/2006	7816	1:11	2 mm Au	515	9150	250
06/25/2006	7840	3:40	2 mm Au	515	9150	250
06/25/2006	7841	2:23	2 mm Au	515	9150	250
06/25/2006	7842	2:23	2 mm Au	515	9150	250
06/25/2006	7843	2:18	2 mm Au	515	9150	250
06/26/2006	7844	2:17	2 mm Au	515	9150	250
06/26/2006	7845	0:46	2 mm Au	515	9150	250
06/23/2006	7827	4:23	4 mm Au	0	515	250
06/24/2006	7828	4:25	4 mm Au	0	515	250
06/24/2006	7829	2:07	4 mm Au	0	515	250
06/23/2006	7824	2:12	4 mm Au	515	9150	250
06/23/2006	7825	2:14	4 mm Au	515	9150	250
06/23/2006	7826	1:20	4 mm Au	515	9150	250
06/08/2006	7588	1:26	7 mm Au	0	9150	250
06/08/2006	7589	1:38	7 mm Au	0	9150	250
06/08/2006	7590	1:45	7 mm Au	0	9150	250
06/08/2006	7591	1:43	7 mm Au	0	9150	250
06/08/2006	7592	1:38	7 mm Au	0	9150	250
06/08/2006	7593	0:36	7 mm Au	0	9150	250
06/08/2006	7594	2:04	7 mm Au	515	9150	250
06/08/2006	7595	2:08	7 mm Au	515	9150	250
06/08/2006	7596	2:02	7 mm Au	515	9150	250
06/24/2006	7830	3:37	10 mm Au	0	515	250
06/24/2006	7831	2:16	10 mm Au	0	515	250
06/24/2006	7832	2:05	10 mm Au	515	9150	250
06/24/2006	7833	2:07	10 mm Au	515	9150	250
06/24/2006	7834	2:03	10 mm Au	515	9150	250
06/24/2006	7835	1:11	10 mm Au	515	9150	250
06/23/2006	7819	0:53	15 mm Au	0	515	250
06/23/2006	7820	1:52	15 mm Au	0	515	250
06/23/2006	7821	0:35	15 mm Au	0	515	250
06/23/2006	7822	2:17	15 mm Au	515	9150	250
06/23/2006	7823	0:47	15 mm Au	515	9150	250
06/22/2006	7811	2:01	20 mm Au	0	515	250
06/22/2006	7812	2:26	20 mm Au	515	9150	250
06/22/2006	7813	0:47	20 mm Au	515	9150	250
07/07/2006	7996	1:54	Mylar backing	0	515	250
07/21/2006	8107	2:32	Mylar backing	0	9150	250
07/21/2006	8108	1:32	Mylar backing	0	9150	250

Table 3: Sample run information. All runs were completed in continuous mode. The livetime provided applies to each delay.

neutron capture reaction. An example of the ESum plot for run 7594 appears in Figure 3. Using this plot, we chose a few potential gates for summed energies using different intervals with the goal of maximizing the ratio of gold events to background events. A comparison of three different gatings appears in Figure 4, which plots the resulting neutron energies near gold's resonance at 4.9 eV.

Figure 5 shows three ESum gates again, but this time normalized to gold data from the Evaluated Nuclear Data File (ENDF) run by Brookhaven National Laboratory. This plot led us to decide on the gate range of 5.3–6.0 MeV because of the reduced background.

3.2 Multiplicity

The DANCE array is able to separate events based on their multiplicity. Neighboring crystals fired during an event are combined to one single cluster in order to make corrections for cross-talking. Gold capture events occur most frequently at multiplicity 3, so we tried three cluster gates including multiplicity 3 in order to determine the optimal gating. Figure 6 shows the summed γ-energy for three different gatings. This analysis revealed that gating on multiplicities 3–4 preserved many of the gold capture events while eliminating most of the events caused by other sources.

3.3 Cross-section gating

We made one final set of cuts in order to examine specific regions of gold's cross-section spectrum, focusing on the first two resonances and the low-energy thermal region. These gates are provided in Table 4.

Au event	E_{min} (eV)	E_{max} (eV)
4.9 eV resonance	4.85	4.95
60.3 eV resonance	60.1	60.9
0.025 eV thermal	0.024	0.026

Table 4: Gold events used to determine beam profile and corresponding energy regions.

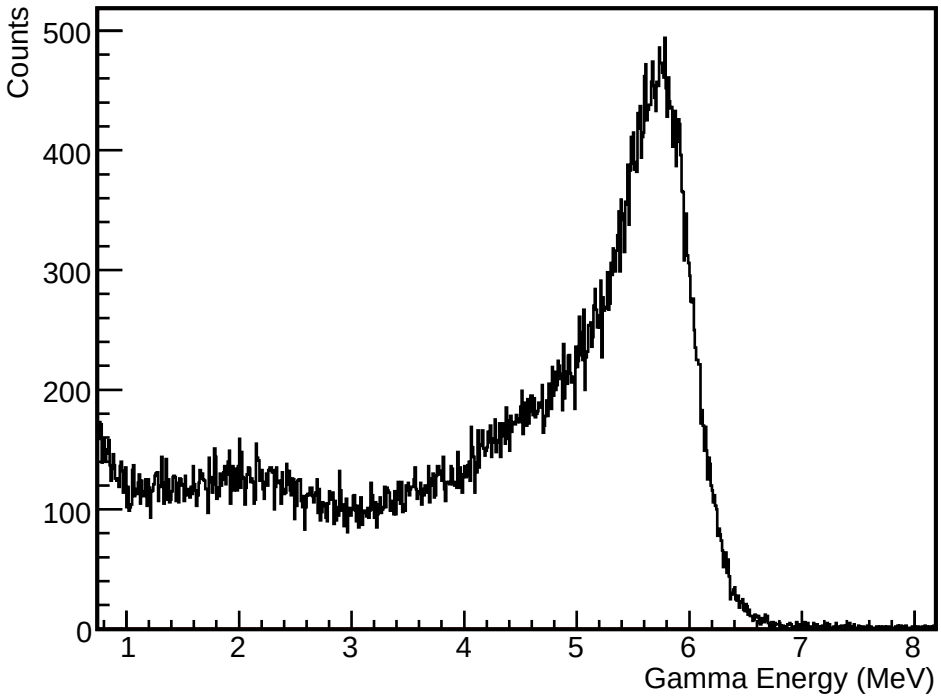

Figure 3: ESum data for run 7594. The events related to gold occur below gold's Q-value of 6.51 MeV for several reasons. One or more γ-rays might have escaped the detector, some of the de-excitations in the cascade can happen by internal conversion and the conversion electrons become absorbed in the material between the sample and the detector, and isomeric states in the decay cascade with long-enough lifetimes do not fall into the coincindence window.

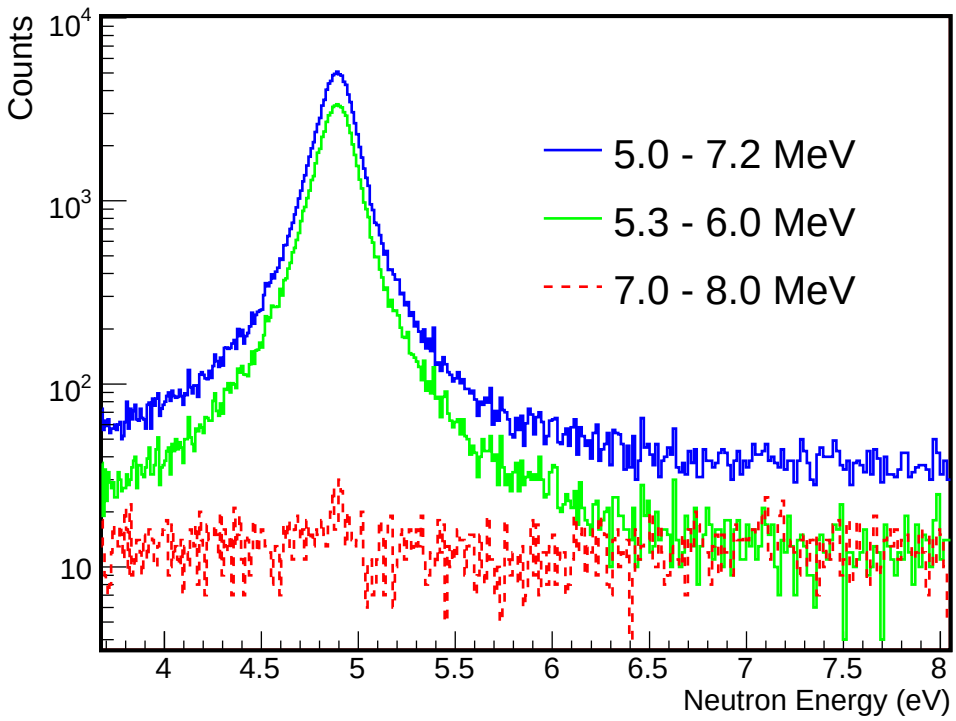

Figure 4: Neutron energy gated by different ESums for run 7594. Shown are the neutron energies near gold's resonance of 4.9 eV. The 5.0-7.2 MeV gate includes the gold peak as well as background above gold's Q-value of 6.51 MeV, while the 5.3–6.0 MeV gate encompasses only gold's peak below the Q-value. While slightly lowering the total counts at the gold resonance peak, the 5.3–6.0 eV gate has less background above $\sim$6 eV. The dashed curve, with gating 7.0–8.0 MeV, serves as an illustration of a gate outside the γ-energy of gold events; what results is almost pure background.

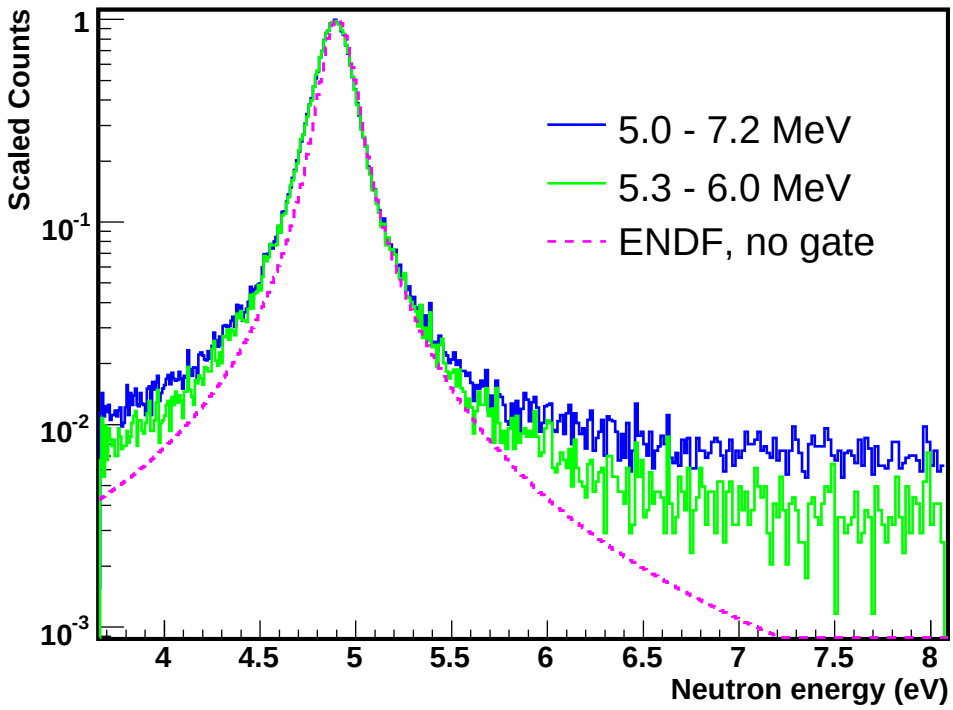

Figure 5: Neutron energy gated by different ESums for run 7594 compared with ENDF data. Shown are the neutron energies near gold's resonance of 4.9 eV. The two solid curves show successively smaller background above ∼6 eV. The dashed curve represents data from ENDF. The three curves are normalized so that they have the same integrated counts from 4.85–4.95 eV (the same range as that used later for the determination of the beam profile) and so that the ENDF curve has its maximum value at 1. Even when normalized, the 5.3–6.0 MeV gate continues to show reduced backgroud away from the resonance at 4.9 MeV.

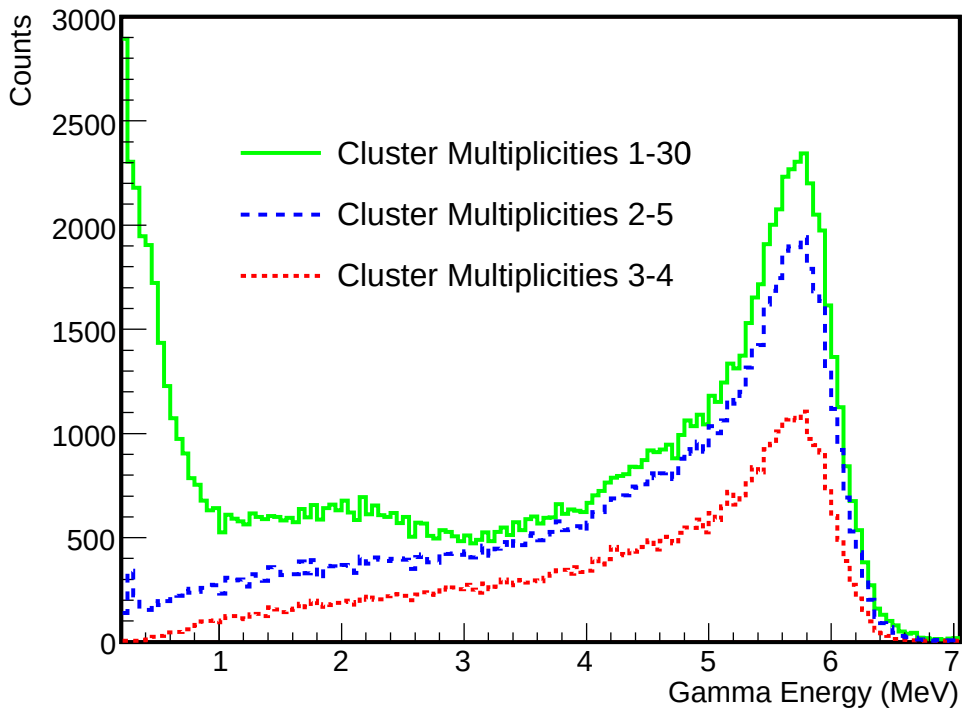

Figure 6: Summed γ-energy for run 7594 with three different cluster-multiplicity gatings. The narrowist cluster-multiplicity, 3–4, preserved the gold peak below its Q-value and eliminated many low-energy events related to background.

3.4 Background

In addition to taking measurements on each gold disc, we measured a sample that included only the Mylar used to hold each gold disc in the aluminum mount. The data for this sample represent the background that we potentially subtract from the gold measurements.

In calculating the flux per unit area, we use a scaled value of the total neutron-monitor counts by considering counts from the uranium neutron-monitor in the time-of-flight interval from 10 μs to 1 ms, which corresponds to energies from 2.15 eV to 21.5 keV. We did not include the first 10 μs of time-of-flight measurements, which include all energies above 21.5 keV. These values fall in the first time-of-flight histogram bin, which, for most runs, has an extremely large number of counts because of high-energy events associated with the so-called gamma flash, which refers to the γ-rays produced when protons hit the tungsten target.

Although we measured the contributions from the background sample for all three energy regions of interest, the background contributions near the 4.9 eV and 60.3 eV resonances were negligible. Figure 7 shows the ESum counts that remain after gating neutron energy between 4.85 and 4.95 eV, and Figure 8 shows the ESum counts that remain after gating neutron energy between 60.1 and 60.9 eV. In these two plots, the counts are at most two or three, which can be attibuted to random events and not actual events generated by the background in this energy region. Thus, we did not need to consider the contributions from the background in analyzing the beam profile near the first two gold resonances.

However, the background does have a significant contribution in the thermal region around 0.025 eV. Figure 9 shows the ESum counts that remain after gating neutron energy between 0.0245 and 0.0255 eV. We attribute these counts not to the Mylar iteself but events apparent only at low energies, including cosmic rays and internal decays of BaF_2. Additionally, the thermal window of interest, as shown Table 4, has a time-of-flight length $\sim$40 times longer than that for region of interest for the 4.9 eV resonance, which means that there was much more time for background- and beam-related events to reveal themselves in the thermal region. That such a background spectrum exists reveals that we had to subtract this background from each of our gold measurements in the gold region. In order to subtract the right amount of the background, we first scaled this

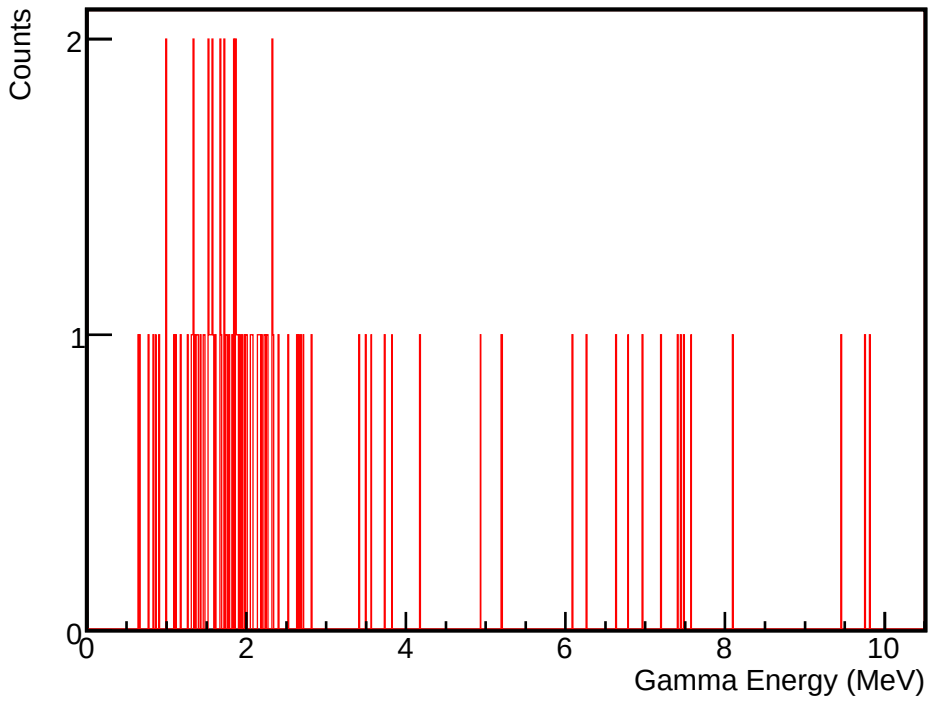

Figure 7: ESum gated around 4.9 eV for background sample. Plotted is the total γ-energy for multiplicities 3–4 gated by neutron energies between 4.85 and 4.95 eV. The plot shows that the background sample contributes negligibly in this energy region.

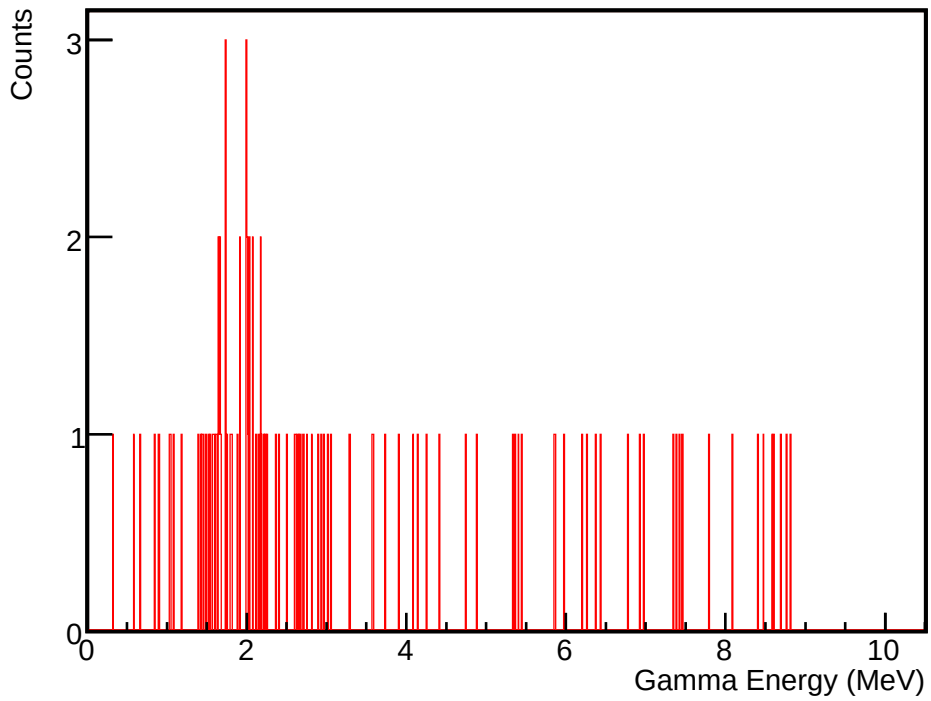

Figure 8: ESum gated around 60.3 eV for background sample. Plotted is the total γ-energy for multiplicities 3–4 gated by neutron energies between 60.1 and 60.9 eV. The plot shows that the background sample contributes negligibly in this energy region.

spectrum and the thermal spectra for the gold samples by the reciprocal of the time integrated number of neutron counts from the uranium neutron-monitor. Then, for each ESum spectra, we calculated the integrated number of counts in the energy window between 1.8 and 2.2 MeV, which encompasses most of the peak resulting from the background sample that is centered at 2.0 MeV. We divded the value of the integral for each gold sample by the integral for the background sample, which generated a scaling factor by which we needed to multiply the background. Table 5 shows the scaling factors for each gold sample in the thermal region. Figure 10 juxtaposes the scaled background with the gold spectrum from which we later subtracted the background contribution. Figure 11 shows the results of the subtraction of the scaled background from the gold samples.

3.5 Flux calculations in concentric discs

Because the Mylar did not contribute significantly to the spectra in the resonance regions, we determined the flux in each gold disc these regions as follows. First, we divided the number of counts in neutron spectra given in Figure 4 by the time-integrated number of neutron counts from the uranium detector. We divided this value by the area of the disc to generate a flux per unit area and by the number of gold atoms:

$$\Phi_{\text{disc}} = \frac{4}{\pi d^2 N_{\text{Au}}} \frac{C_{\text{Au}}}{C_{\text{U}}} \ , \tag{3}$$

with statistical uncertainty

$$\sigma_{\Phi} = \frac{4}{\pi d^2 N_{\text{Au}}} \frac{C_{\text{Au}}}{C_{\text{U}}} \sqrt{\frac{1}{C_{\text{Au}}} + \frac{1}{C_{\text{U}}}} \ . \tag{4}$$

Here, C_{Au} is the number of counts in the region of interest, C_{U} is the number of counts from the uranium neutron-monitor, N_{Au} the number of gold atoms per square centimeter gold foil, and d is the gold sample's diameter.

For the thermal region, which had significant contributions from the Mylar, we multiplied the scaling factor given in Table 5 by the quotient of the total events in the region of interest for the Mylar sample and the time-integrated number of neutron counts from the uranium neutron-monitor. We divided this value by the area of the disc to generate a flux per unit area and by the number of gold atoms:

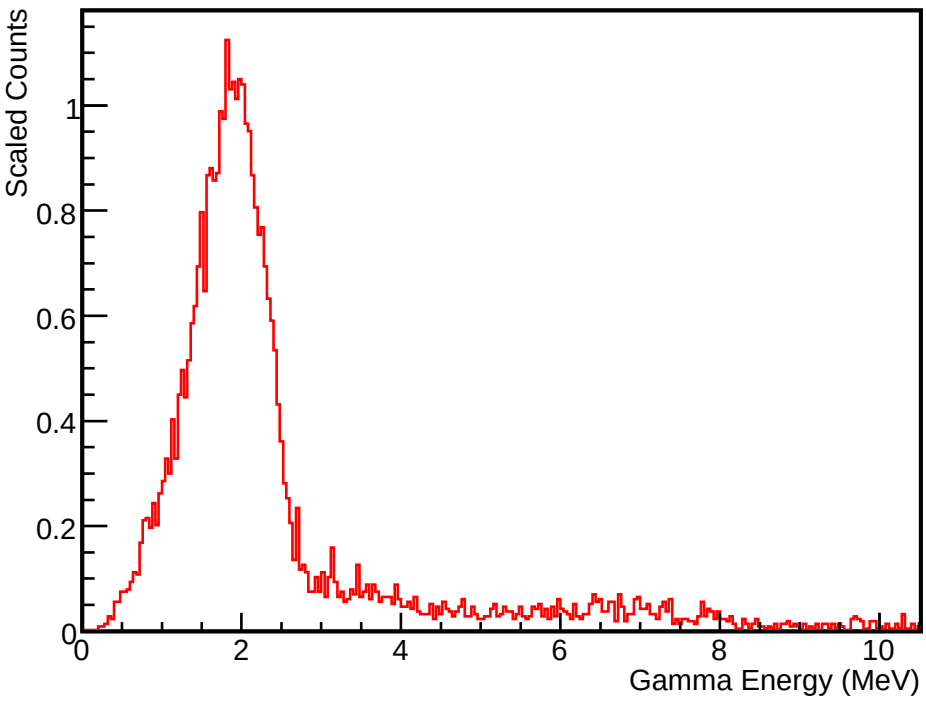

Figure 9: ESum gated around 0.025 eV for Mylar sample. Plotted is the total γ-energy for multiplicities 3–4 gated by neutron energies between 0.0245 and 0.0255 eV. The plot shows that the Mylar sample has a significant contribution in the thermal region.

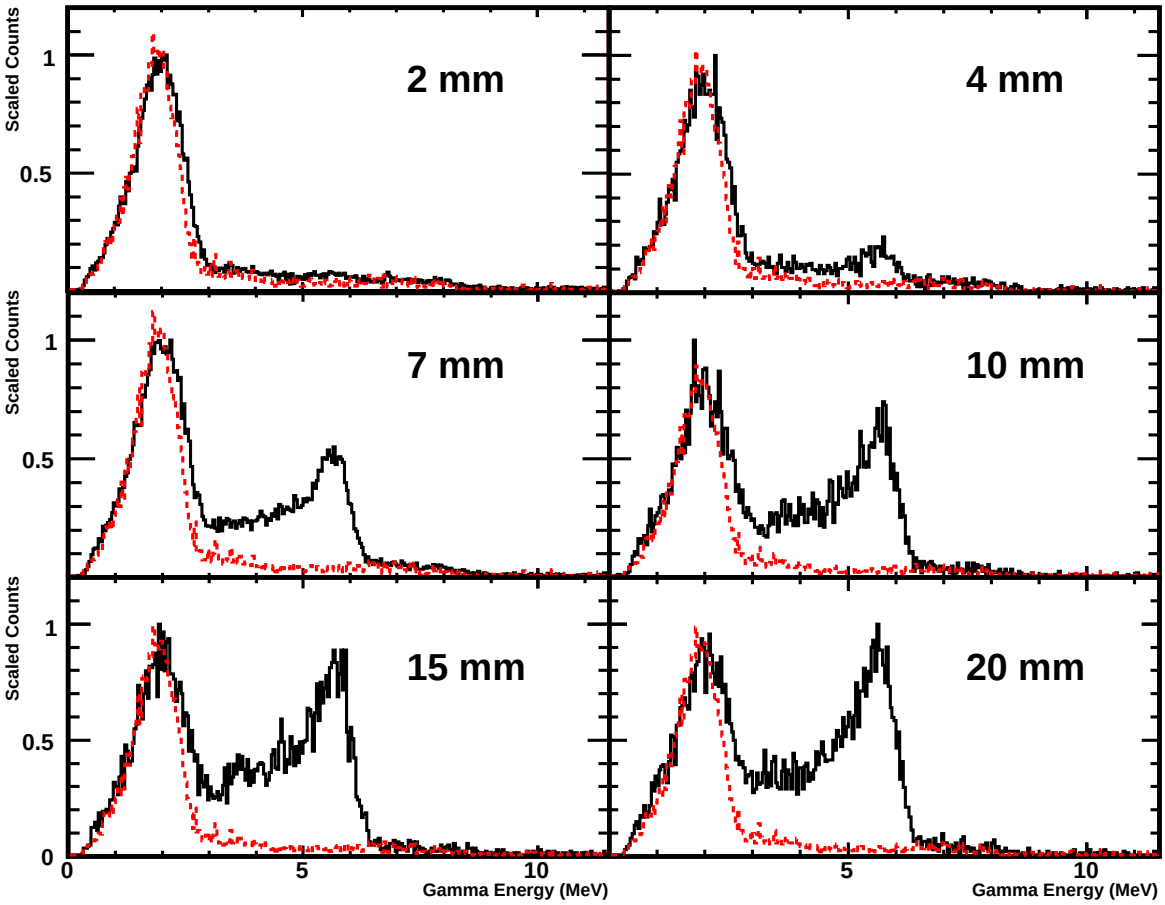

Figure 10: ESum gated around 0.025 eV for scaled background sample and gold samples. The dashed plots are the background that has been scaled to the solid gold plots. The scalings force the number of counts between 1.8 and 2.2 eV for the background and for each gold sample to be equal, and the two plots are renormalized to the smallest sample.

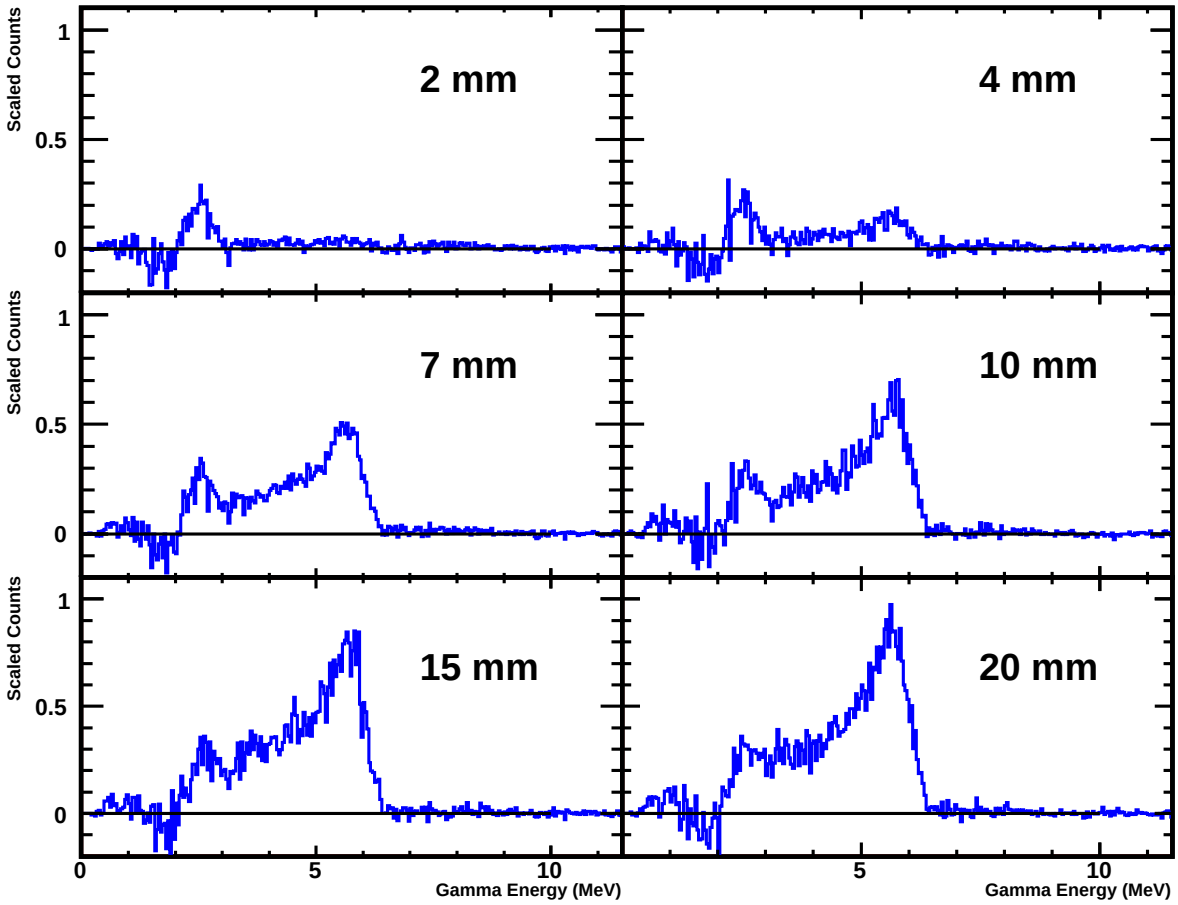

Figure 11: Subtraction of scaled background from gold samples. The graphs show the difference between the solid and dashed histograms in Figure 10. As the gold diameter increases, the gold events below gold's Q-value of 6.51 MeV become more visible.

$$\Phi_{\text{disc}} = \frac{4}{\pi d^2 N_{\text{Au}}} \left[\left(\frac{C_{\text{Au}}}{C_{\text{U}}} \right) - k \left(\frac{M_{\text{Au}}}{M_{\text{U}}} \right) \right] , \tag{5}$$

with statistical uncertainty

$$\sigma_{\Phi} = \frac{4}{\pi d^2 N_{\text{Au}}} \sqrt{\frac{C_{\text{Au}}^2}{C_{\text{U}}^2} \left(\frac{1}{C_{\text{Au}}} + \frac{1}{C_{\text{U}}} \right) + k^2 \left[\frac{M_{\text{Au}}^2}{M_{\text{U}}^2} \left(\frac{1}{M_{\text{Au}}} + \frac{1}{M_{\text{U}}} \right) \right]} . \tag{6}$$

C_{Au} is the number of counts in the region of interest for the gold sample, C_{U} is the number of counts from the uranium neutron-monitor for the gold sample, M_{Au} is the number of counts in the gold region of interest for the Mylar sample, M_{U} is the number of counts from the uranium neutron-monitor for the Mylar sample, k is the background scaling factor in Table 5, N_{Au} the number of gold atoms per square centimeter gold foil, and d is the gold sample's diameter. All the values for C_{Au}, C_{U}, M_{Au}, and M_{U} are given in Table 5. The fluxes for each disc near the resonances as well as in the thermal region are provided in Table 6.

Figure 12 displays the fluxes of each disc in each of the three examined gold regions.

3.6 Flux calculations in concentric annuli

We also computed the beam profile using a differential method that generates the flux for annular regions. To determine the profile near the gold resonances, we calculated the number of gold events per neutron monitor event for an entire gold sample, subtracted the number of gold events per neutron monitor event for the next smallest sample, and divided that value by the area of the corresponding annulus:

$$\Phi_{\text{annulus}} = \frac{4}{\pi (d_2^2 - d_1^2)} \left(\frac{C_{\text{Au}_2}}{C_{\text{U}_2} N_{\text{Au}_2}} - \frac{C_{\text{Au}_1}}{C_{\text{U}_1} N_{\text{Au}_1}} \right) , \tag{7}$$

where C_{Au} is the number of gold counts in the region of interest, and C_{U} are the number of neutron-monitor events in the 10 μs to 1 ms interval. Subscript 1 refers to the inner disc, while subscript 2 refers to the outer disc. The statistical uncertainties for the fluxes are given by:

$$\sigma_{\Phi} = \frac{4}{\pi (d_2^2 - d_1^2)} \sqrt{\frac{C_{\text{Au}_2}^2}{C_{\text{U}_2}^2 N_{\text{Au}_2}^2} \left(\frac{1}{C_{\text{Au}_2}} + \frac{1}{C_{\text{U}_2}} \right) + \frac{C_{\text{Au}_1}^2}{C_{\text{U}_1}^2 N_{\text{Au}_1}^2} \left(\frac{1}{C_{\text{Au}_1}} + \frac{1}{C_{\text{U}_1}} \right)} . \tag{8}$$

Energy region	Sample	C_{Au}	C_{U}	B_{Au}	B_{U}	k
4.85–4.95 eV	2 mm	13,812	1,163,430	–	–	N/A
	4 mm	14,987	310,279	–	–	N/A
	7 mm	40,063	287,281	–	–	N/A
	10 mm	32,830	131,555	–	–	N/A
	15 mm	84,550	243,696	–	–	N/A
	20 mm	61,415	169,283	–	–	N/A
	Background	–	–	3	66,935	–
60.1–60.9 eV	2 mm	219	453,191	–	–	N/A
	4 mm	196	101,469	–	–	N/A
	7 mm	2,215	391,081	–	–	N/A
	10 mm	198	21,463	–	–	N/A
	15 mm	1,976	135,818	–	–	N/A
	20 mm	935	59,558	–	–	N/A
	Background	–	–	7	226,804	–
0.024–0.026 eV	2 mm	1,171	710,236	–	–	0.718
	4 mm	852	208,810	–	–	0.737
	7 mm	6,983	678,362	–	–	0.692
	10 mm	1,893	110,092	–	–	0.787
	15 mm	2,509	107,878	–	–	0.882
	20 mm	2,676	109,725	–	–	0.850
	Background	–	–	191	159,869	–

Table 5: Count values for different energy windows and samples. C_{Au} represents the number of neutron counts in the gold energy regions of interest, while C_{U} is the time-integrated number of counts from the uranium neutron-monitor. B_{Au} and B_{U} are represent the same values but for the background sample. The counts for the background sample in energy regions 4.85–4.95 eV and 60.1–60.9 eV are negligible. The k-values are the scaling factors by which we multiplied the background before subtracting it from the gold counts.

Au event	r (mm)	Φ_{disc}
4.9 eV resonance	1.0	1.000(9)
	2.0	1.028(9)
	3.5	0.996(5)
	5.0	0.877(5)
	7.5	0.551(2)
	10.0	0.327(2)
60.3 eV resonance	1.0	1.00(7)
	2.0	0.01(7)
	3.5	0.99(2)
	5.0	0.80(6)
	7.5	0.57(1)
	10.0	0.35(1)
0.025 eV thermal	1.0	1.00(10)
	2.0	1.98(5)
	3.5	0.10(1)
	5.0	0.91(2)
	7.5	0.55(1)
	10.0	0.330(6)

Table 6: Fluxes per unit area for circular regions of DANCE beam. Each flux Φ is for a disc of radius r and is normalized to the smallest sample.

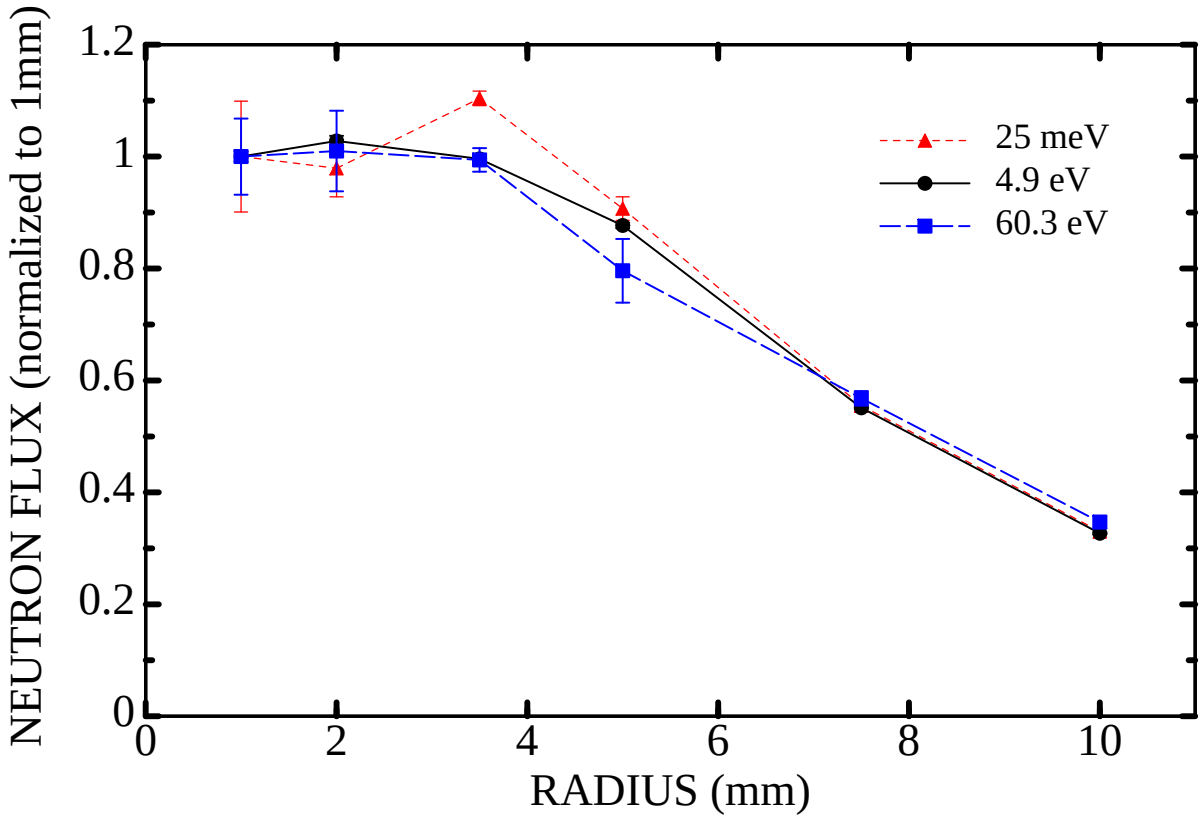

Figure 12: Flux for each gold disc calculated from the three different energy regions described in the text. The data points are plotted as the outer edge of the discs. The vertical error bars, resulting from statistical uncertainties due to different number of counts for each gold disc measured, are sometimes smaller than the marker size. The data are normalized to the smallest sample.

Table 7 shows the data for the different annular regions.

We followed a similar method for the thermal region but first subtracted the scaled value of the ratio of counts in the region of interest to total uranium counts for the Mylar sample:

$$\Phi_{\text{annulus}} = \frac{4}{\pi(d_2^2 - d_1^2)} \left\{ \left[\frac{C_{\text{Au}_2}}{C_{\text{U}_2} N_{\text{Au}_2}} - k_2 \left(\frac{B_{\text{Au}}}{B_{\text{U}}} \right) \right] - \left[\frac{C_{\text{Au}_1}}{C_{\text{U}_1} N_{\text{Au}_1}} - k_1 \left(\frac{B_{\text{Au}}}{B_{\text{U}}} \right) \right] \right\} , \tag{9}$$

where C_{Au} is the number of counts in the region of interest for the gold sample, C_{U} is the number of counts from the uranium neutron-monitor for the gold sample, B_{Au} is the number of counts in the gold region of interest for the Mylar sample, B_{U} is the number of counts from the uranium neutron-monitor for the Mylar sample, k is the background scaling factor in Table 5, and d is the gold sample's diameter. Subscript 1 refers to the inner disc, while subscript 2 refers to the outer disc. The statistical uncertainties for the fluxes are given by:

$$\sigma_\Phi = \frac{4}{\pi(d_2^2 - d_1^2)} \sqrt{\frac{C_{\text{Au}_2}^2}{C_{\text{U}_2}^2 N_{\text{Au}_2}^2} \left(\frac{1}{C_{\text{Au}_2}} + \frac{1}{C_{\text{U}_2}} \right) + (k_2^2 + k_1^2) \left[\frac{B_{\text{Au}}^2}{B_{\text{U}}^2} \left(\frac{1}{B_{\text{Au}}} + \frac{1}{B_{\text{U}}} \right) \right] + \frac{C_{\text{Au}_1}^2}{C_{\text{U}_1}^2 N_{\text{Au}_1}^2} \left(\frac{1}{C_{\text{Au}_1}} + \frac{1}{C_{\text{U}_1}} \right)} . \tag{10}$$

Table 7 shows the data for the different annuli in the thermal region.

Figure 13 displays the beam profile in each of the three examined regions. Figures 14 and 15 compare the profile as generated by gold's 4.9 eV resonance and by gold's 60.3 resonance and by gold's 4.9 eV resonance and in the thermal region, respectively.

4 Discussion

We successfully characterized the profile of the DANCE neutron beam in three different energy regions, from the low-energy thermal region to ∼100 eV. The profile in each of the examined energy regions reveals a full-width-half-maximum value for the relative neutron flux to occur at beam radius 5 mm, which is consistent with previous estimates. However, our results show a shallower dropoff of the beam at larger radii, which contrasts with previous theoretical calculations that show an extremely steep dropoff starting at ∼5 eV.

Au event	r (mm)	Φ_{annulus}
4.9 eV resonance	0–1.0	1.000(9)
	1.0–2.0	1.037(12)
	2.0–3.5	0.981(9)
	3.5–5.0	0.762(12)
	5.0–7.5	0.291(6)
	7.5–10.0	0.038(5)
60.3 eV resonance	0–1.0	1.00(7)
	1.0–2.0	1.01(10)
	2.0–3.5	0.99(5)
	3.5–5.0	0.61(11)
	5.0–7.5	0.39(5)
	7.5–10.0	0.06(3)
0.025 eV thermal	0–1.0	1.00(11)
	1.0–2.0	1.03(7)
	2.0–3.5	1.01(3)
	3.5–5.0	0.71(4)
	5.0–7.5	0.27(4)
	7.5–10.0	0.04(2)

Table 7: Flux per unit area for annular regions of neutron beam. Each flux Φ is for an annulus with radii r and is normalized to the smallest sample.

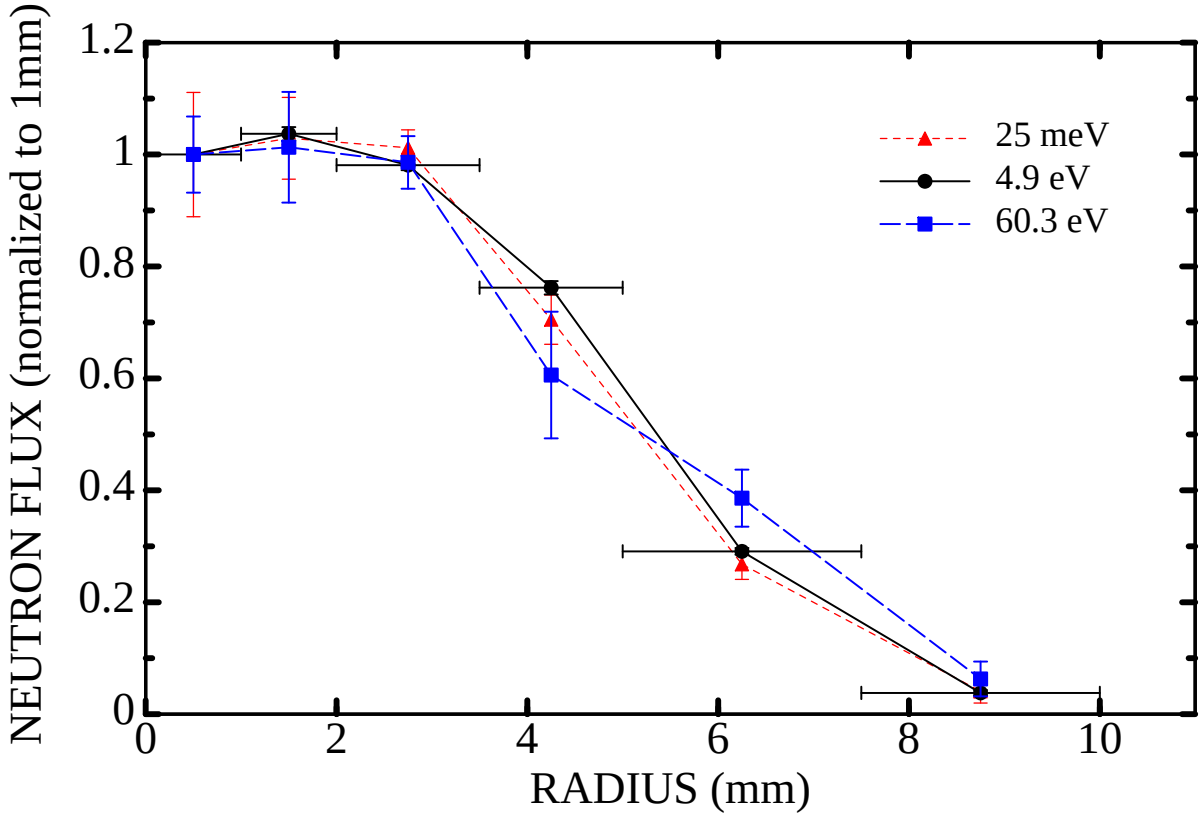

Figure 13: Beam profile as a function of radius calculated from the three different energy regions described in the text. The data points are plotted as the center of the annulus, and the horizontal bars for the 4.9 eV case cover the span of the annuli. The vertical error bars, resulting from statistical uncertainties due to different number of counts for each gold disc measured, are sometimes smaller than the marker size. The data are normalized to the smallest sample.

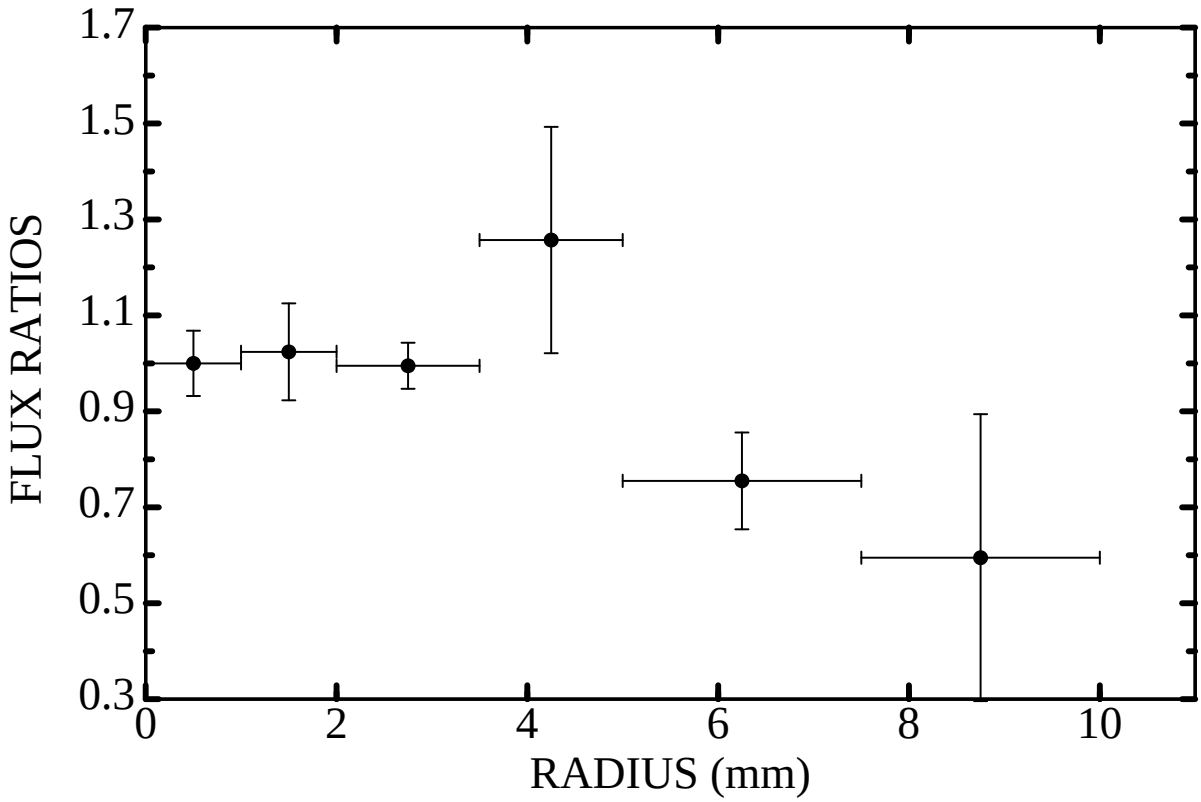

Figure 14: Beam profile comparison for 4.9 eV and 60.3 eV. Shown are the ratios of the profile generated by the 4.9 eV resonance to the profile generated by the 60.3 eV resonance. The data points are plotted as the center of the annulus, and the horizontal bars cover exactly the span of the annuli. The vertical error bars result from statistical uncertainties as a result of the different number of counts for each gold disc measured. The data are normalized to the smallest sample. The closer the subsequent values are to the value of 1, the more agreement there exists between the beam profile determined by the first two gold resonances.

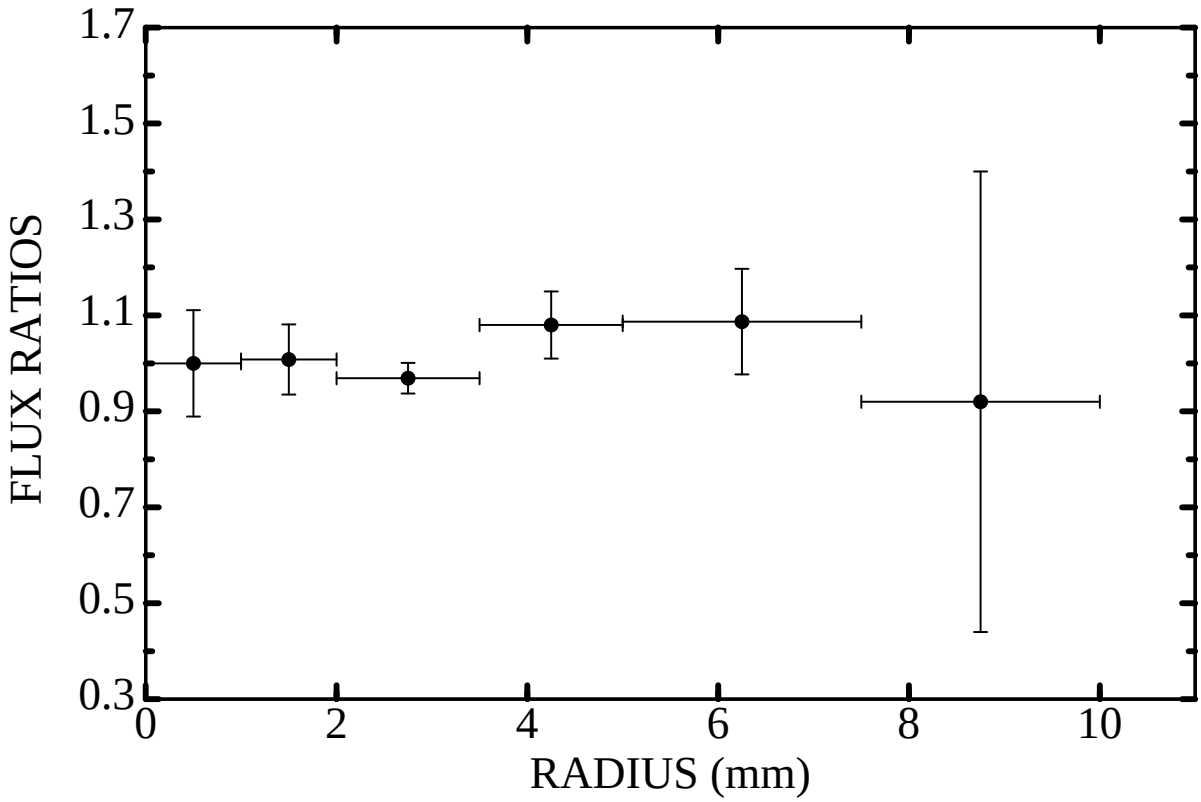

Figure 15: Beam profile comparison for 4.9 eV and 0.025 eV. Shown are the ratios of the profile generated by the 4.9 eV resonance to the profile generated for the 0.025 eV thermal region. The data points are plotted as the center of the annulus, and the horizontal bars cover the span of the annuli. The vertical error bars result from statistical uncertainties as a result of the different number of counts for each gold disc measured. The data are normalized to the smallest sample. The closer the subsequent values are to the value of 1, the more agreement there exists between the beam profile determined by the first gold resonance and the thermal region.